Journal of Applied Physics ARTICLE scitation.org/journal/jap

Dynamically morphing microchannels in liquid crystal elastomer coatings containing disclinations

Cite as: J. Appl. Phys. **128**, 184702 (2020); doi: 10.1063/5.0022193
Submitted: 17 July 2020 · Accepted: 23 October 2020 ·
Published Online: 12 November 2020

View Online Export Citation CrossMark

Greta Babakhanova,[1,2] Youssef M. Golestani,[1,2] Hend Baza,[3] Sajedeh Afghah,[3] Hao Yu,[1,2] Michael Varga,[1,2] Qi-Huo Wei,[1,2] Paul Shiller,[4] Jonathan V. Selinger,[1,2,3] Robin L. B. Selinger,[1,2,3,a)] and Oleg D. Lavrentovich[1,2,3,a)]

AFFILIATIONS

[1]Advanced Materials and Liquid Crystal Institute, Kent, Ohio 44242, USA
[2]Materials Science Graduate Program, Kent State University, Kent, Ohio 44242, USA
[3]Department of Physics, Kent State University, Kent, Ohio 44242, USA
[4]Civil Engineering-Timken Engineered Surface Laboratory, The University of Akron, Akron, Ohio 44325, USA

Note: This paper is part of the Special Topic on Programmable Liquid Crystal Elastomers.

[a)]**Authors to whom correspondence should be addressed:** rselinge@kent.edu and olavrent@kent.edu

ABSTRACT

Liquid crystal elastomers (LCEs) hold a major promise as a versatile material platform for smart soft coatings since their orientational order can be predesigned to program a desired dynamic profile. In this work, we introduce temperature-responsive dynamic coatings based on LCEs with arrays of singular defects-disclinations that run parallel to the surface. The disclinations form in response to antagonistic patterns of the molecular orientation at the top and bottom surfaces, imposed by the plasmonic mask photoalignment. Upon heating, an initially flat LCE coating develops linear microchannels located above each disclination. The stimulus that causes a non-flat profile of LCE coatings upon heating is the activation force induced by the gradients of molecular orientation around disclinations. To describe the formation of microchannels and their thermal response, we adopt a Frank–Oseen model of disclinations in a patterned director field and propose a linear elasticity theory to connect the complex spatially varying molecular orientation to the displacements of the LCE. The thermo-responsive surface profiles predicted by the theory and by the finite element modeling are in good agreement with the experimental data; in particular, higher gradients of molecular orientation produce a stronger modulation of the coating profile. The elastic theory and the finite element simulations allow us to estimate the material parameter that characterizes the elastomer coating's response to the thermal activation. The disclination-containing LCEs show potential as soft dynamic coatings with a predesigned responsive surface profile.

I. INTRODUCTION

Soft coatings with stimuli-responsive topographies attract considerable research interest, triggered by a wide range of potential applications.[1–5] Surface topography defines many useful properties of a coating, including optical reflection, wettability, friction, adhesion, and an ability to control adjacent media such as biological cell cultures.[6–9] Tremendous progress has been achieved in understanding and designing static coatings. The current challenge is to design coatings with a dynamic response to various chemical and physical cues. Among many potential candidates, liquid crystal elastomers (LCEs) show several advantages over other materials, thanks to the coupling of their rubber-like elasticity to the intrinsic orientational order.[10–13] This coupling enables a broad platform for the design of elastic response of LCE coatings to various external cues that modify the orientational order.

The orientational order is specified by its amplitude, called the scalar order parameter S that describes how well the molecular entities are aligned along the preferred direction, and its phase,

called the director $\hat{\mathbf{n}}$ ($|\hat{\mathbf{n}}| = 1$, $\hat{\mathbf{n}} \equiv -\hat{\mathbf{n}}$) that is the local preferred direction of orientation.[14] Modification of both S and $\hat{\mathbf{n}}$ produces an elastic response of an LCE. For example, heat actuation of a uniform LCE film, $\hat{\mathbf{n}}(\mathbf{r}) = \text{const.}$, leads to a uniform contraction-stretching, shrinking the film along the director and expanding it in the two perpendicular directions.[15,16] The effect is caused by the decrease in S as the temperature is raised;[16] it is of interest for the development of artificial muscles.[15] Even more exciting opportunities are offered by the director that changes in space, $\hat{\mathbf{n}}(\mathbf{r}) \neq \text{const}$. In particular, thin LCE films with in-plane director patterns, when free of any substrates, develop thermally activated 3D shape changes with non-trivial mean and Gaussian curvatures,[4,17–21] while director deformations across the LCE films trigger oscillations[22] and locomotion[23] when activated by light.

In LCE coatings, prepared with one surface free and another clamped to a substrate, the spatially varying director field causes topographical changes under the influence of various cues, such as temperature,[20,24–26] light,[18,21–23,27] electric field, humidity,[8,28–31] etc. For example, using chiral liquid crystal precursors, Liu and co-workers realize dynamic topographies of LCE coatings with rectilinear[3] and "fingerprint"[32] topographies for applications such as dust removal. Recent studies[24,26] demonstrate that the dynamic surface profile of the LCE surfaces could be deterministically predesigned by imposing in-plane deformations of the director $\hat{\mathbf{n}}(x, y)$. In particular, bend $\mathbf{B} = \hat{\mathbf{n}} \times \text{curl}\,\hat{\mathbf{n}}$ causes elevations of the LCE profile upon heating, while splay $\mathbf{S} = \hat{\mathbf{n}}\text{div}\,\hat{\mathbf{n}}$ produces indentations. These topography changes are related to the "activation force" $\mathbf{f} = \alpha|\Delta S|(\hat{\mathbf{n}}\text{div}\,\hat{\mathbf{n}} - \hat{\mathbf{n}} \times \text{curl}\,\hat{\mathbf{n}})$ that triggers displacements of LCE in response to the heating-induced decrease of S by $|\Delta S|$ within the pattern with the director gradients; $\alpha > 0$ is the elastic parameter of the LCE.[24]

Motivated by the deterministic relationship between the underlying patterns of molecular orientation and the dynamic surface topography of LCE coatings, in this work, we explore a complex three-dimensional geometry of the preinscribed director field. Namely, the director field is predesigned to change in the plane of the LCE coating and along the normal to it with the goal to produce singular lines, the so-called disclinations, that run parallel to the substrate in the bulk of the coating. The disclinations form in response to a predesigned surface orientation of the director at the top and bottom surfaces.[33,34] The interest to the disclinations is explained by the dramatic enhancement of the gradients of $\hat{\mathbf{n}}$ and S near their cores. These strong gradients are expected to enhance the activation forces and modify significantly the profiles of the LCE coatings.

Because of the intricate structure of the LCE coatings, we combine the experiment with analytical and numerical modeling. In the experimental part, we first establish director configurations and locations of disclinations in the bulk of the nematic sample and then use an optical surface profiler and a digital holographic microscope (DHM) to trace the response of the coating topography to temperature changes. We then present an approximate analytical model of the director field and simulate it numerically, using a finite difference method and the Frank–Oseen free energy functional. The study demonstrates that the patterned director field produces sharp microchannels-indentations at the surface of the LCE coating, located above the bulk disclinations. Besides these deflections, appearing as out-of-plane displacements, the coatings also develop in-plane displacements. The experimentally observed shape changes of the LCE coatings correlate with the qualitative consideration of spatial variation of the activation force $\mathbf{f}$ and are well described by the linear elasticity theory and by nonlinear finite-element numerical simulations.

II. MATERIALS AND METHODS

The patterned director field with stable disclinations running through the bulk of the sample parallel to the top and bottom surfaces, Fig. 1, is produced by a method similar to that described by Wang *et al*,[34] namely, by placing the monomeric (non-polymerized) liquid crystal between two glass plates with different surface alignments, uniform planar at one substrate, written in the Cartesian coordinates as $\hat{\mathbf{n}}(x, y, z = 0) = (1, 0, 0)$, and periodically distorted with alternating splay and bend,

$$\hat{\mathbf{n}}(x, y, z = d) = \left(\cos\frac{\pi x}{L},\ \sin\frac{\pi x}{L},\ 0\right), \tag{1}$$

at the opposite plate. Here, d is the cell thickness and L is the period of the director stripe pattern that resembles rows of the letter "C," set to be equal to $40\,\mu$m or $80\,\mu$m, Figs. 1(a) and 1(d). The surface

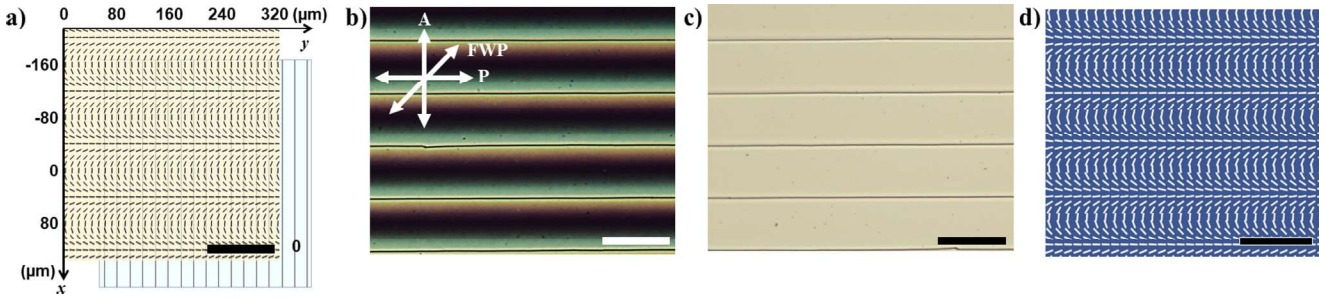

FIG. 1. (a) Scheme of surface treatments to produce lattice of rectilinear freely standing disclinations in a nematic slab; (b) polarizing optical microscope image of an LCE coating equiped with a full wave plate at 45°; (c) bright-field image of the disclinations (unpolarized light); (d) LC-PolScope image of the photopatterned director field map of the "C"-stripe pattern, where the blue color indicates optical retardation of 55 nm. Scale bars, 100 μm. The thickness of the LCE coating in parts (b) and (c) is $d = 6\,\mu$m; the thickness of a spin-coated LCE layer made of RM257 in part (d) is 100 nm.

patterns of $\hat{\mathbf{n}}$ are created by the plasmonic mask technique (Sec. II A). Equation (1) implies pure bend at $x = 0, \pm L, \pm 2L, \ldots$, and splay at $x = \pm\frac{L}{2}, \pm\frac{3L}{2}, \ldots$. As clear from the comparison of the two director configurations at $z = 0$ and $z = d$, the director must reorient by $\pi/2$ as one moves from any point at $x = \pm L/2, \pm 3L/2, \ldots$, from one substrate to another along the normal z axis. This requirement is resolved by the formation of singular disclination lines of strength 1/2 that run along the y axis, with their cores located at $x = \pm L/2, \pm 3L/2, \ldots$. The difference in the director patterns at the $z = 0$ and $z = d$ planes introduces twist deformations along the z axis, which are of opposite handedness on the left-hand and right-hand sides of each disclination. The disclinations and twisted regions are visible under a polarizing microscope with a full-wavelength plate (FWP) used as an optical compensator, Fig. 1(b). The disclinations are well resolved also in unpolarized light, Fig. 1(c), as the director distortions at their cores strongly scatter light.

A. Preparation of the aligning substrates

Glass plates with indium tin oxide (ITO) coatings are cleaned in an ultrasonic bath and subsequently rinsed with isopropyl alcohol. The plates are then dried in an oven and additionally cleaned by the UV/ozone procedure. The planar alignment is achieved by spin coating a polyimide layer PI2555 (HD Microsystems) onto the cleaned plates and baking it in an oven at 275 °C for 1 h, after which the substrates are rubbed 10 times with a velvet cloth in a unidirectional fashion.

The "C"-stripe's director patterns on the plates are produced by a plasmonic meta-mask (PMM) photoalignment.[35] The PMM represents a thin Al film with rectangular $200 \times 100\ \text{nm}^2$ nanoslits arranged into the same "C"-stripe patterns as the desired director field in Eq. (1).[35] The method requires a thin layer of a photosensitive dye molecule that react to light irradiation by realigning their long axes perpendicular to the direction of light polarization. This layer is produced by spin coating a 0.5 wt. % solution of the dye brilliant yellow (BY) (Sigma Aldrich) [Fig. 2(a)] in *N*, *N*-dimethylformamide (DMF) onto the glass and baking the plates at 95 °C for 30 min. An unpolarized light beam emitted by the source EXFO X-Cite series 120, passing through the PMM acquires local linear polarization along the direction perpendicular to the nanoslits. The transmitted light aligns the BY molecules perpendicular to the local polarization direction. The resulting pattern of dye orientation reproduces the director field in Eq. (1). To verify the alignment geometry, we spin coated a very thin (~100 nm) birefringent monomer RM257 [Fig. 2(b)] onto the photopatterned BY layer and imaged the resulting director by LC PolScope, which shows the local orientation of the optic axis [Fig. 1(d)].

Two differently treated plates, one unidirectionally aligned, and one patterned as in Eq. (1), are used to prepare a sandwich-type flat cell [Fig. 1(a)] with the gap spacing controlled by spherical microspacers with a diameter 5, 7, and 17.5 μm (Sekisui Chemical Co. Ltd.) pre-mixed with NOA71 (Norland Products, Inc.) UV glue applied at the periphery of the cell.

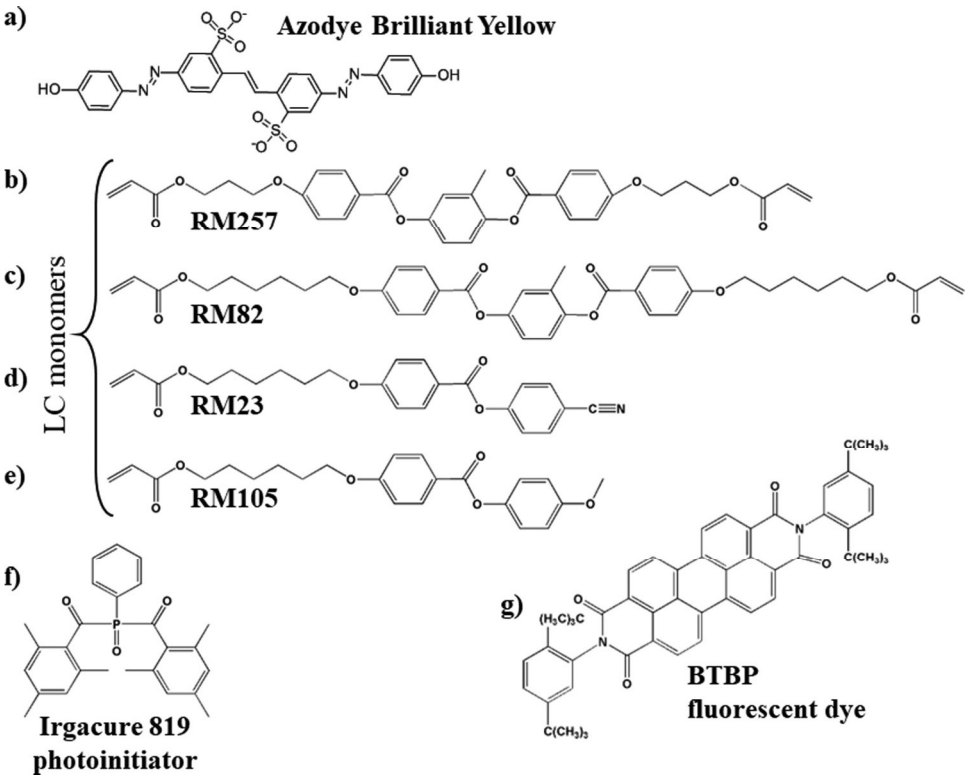

FIG. 2. Chemicals used in the experiment: (a) Azodye brilliant yellow; monomers (b) RM257, (c) RM82, (d) RM23, and (e) RM105; (f) photoinitiator Irgacure 819; (g) fluorescent dye BTBP for fluorescence confocal polarizing microscopy.

B. Materials for elastomer coatings

To form an LCE coating, liquid crystal monomers RM82 (25 wt. %), RM23 (25 wt. %), and RM105 (49.2 wt. %) [Figs. 2(c)–2(e)] are homogeneously mixed with a 0.8 wt. % solution of photoinitiator Irgacure 819 (Merck) [Fig. 2(f)] in dichloromethane (Sigma Aldrich). The mixture is stirred at 40 °C overnight and then injected into a cell in its isotropic phase at 80 °C by capillary action. The cells are cooled to the nematic phase at a rate of 0.5 °C/min and then to 25 °C at 5 °C/min. After the director pattern with the disclinations equilibrates, the samples are photopolymerized using a 365 nm LED light source (Thorlabs M365LP1) for 10 min with an intensity of 183 W/m^2. Once the monomeric mixture is photopolymerized into an LCE with an array of disclinations, one substrate is removed using a razor blade to leave an LCE coating on the second substrate. We investigate two cases, which produce noticeably different results: (1) an LCE coating in which the patterned surface is attached to a photopatterned glass substrate and the uniformly aligned surface is free and (2) an LCE coating in which the uniformly aligned surface is clamped, while the photopatterned side is free. We abbreviate these two cases as "uniform free surface," or UFS, and "patterned free surface," or PFS, respectively. The LCE coatings remain attached to the substrates in all the experiments reported below; no peeling is observed.

C. Fluorescence confocal polarizing microscopy

Optical microscopy shows that the disclinations run along the y axis and are located at $x = \pm L/2, \ \pm 3L/2, \ \ldots$, Figs. 1(b) and 1(c), but it cannot decipher the z-locations of the disclination. To find the z-coordinates, we use fluorescence confocal polarizing microscopy (FCPM).[36] For FCPM imaging, the LC monomeric mixture described above is doped with a ≈0.02 wt. % fluorescent dye *N*, *N*′-bis(2,5-di-*tert*-butylphenyl)-3,4,9,10-perylenedicarboximide (BTBP) (Sigma Aldrich) [Fig. 2(g)]. The BTBP molecules align their long axes parallel to the local director. Chloroform solvent was used to create a homogeneous mixture and left to evaporate overnight at 50 °C in a vacuum oven. The LCE with BTBP was polymerized as described above (Sec. II B). To visualize the 3D director field, an LCE coating is probed with a linearly polarized light at the wavelength of 488 nm (Ar laser). The irradiation causes fluorescence of the BTBP molecules. In the reflection mode of FCPM, the fluorescent signal is transmitted back to a detector through the same polarizer that is used to polarize the probing beam.[36,37] The samples for FCPM imaging were purposefully thicker ($d = 17.5\,\mu$m, Fig. 3) than those in other experiments ($d = 5, 7\,\mu$m) in order to resolve better the locations of disclinations in the xz plane. To improve the image quality, the FCPM observations are performed by placing a small drop of type A immersion oil (Nikon) on top of the LCE coating and using PlanApo 60× objectives with NA of 1.42.

III. RESULTS AND DISCUSSION

A. Experimental results

1. 3D director field and locations of disclination

Fluorescence confocal polarizing microscopy (FCPM) with a controlled direction of the linearly polarized light that probes the LCE coating enables us to map the director field along all three spatial dimensions. The FCPM textures of a PFS LCE coating ($d = 17.5\,\mu$m) are shown in Fig. 3. The in-plane xy-texture [Fig. 3(a)] with the polarizer along the x axis clearly identifies the regions $x = 0, \ \pm L, \ \pm 2L, \ \ldots$ of bend as the regions of the highest FCPM intensity, since in these regions the local director and the BTBP molecules are oriented along the x axis. The disclinations appear as sharp lines in the splay regions $x = \pm L/2, \ \pm 3L/2, \ \ldots$. The cross-sectional xz-textures of the PFS LCE coating acquired with the polarization of probing beam along the x- and y-directions are presented in Figs. 3(b) and 3(c), respectively. In Fig. 3(b), the bend regions exhibit the highest intensity of fluorescent signal, while the disclination cores appear in the dark

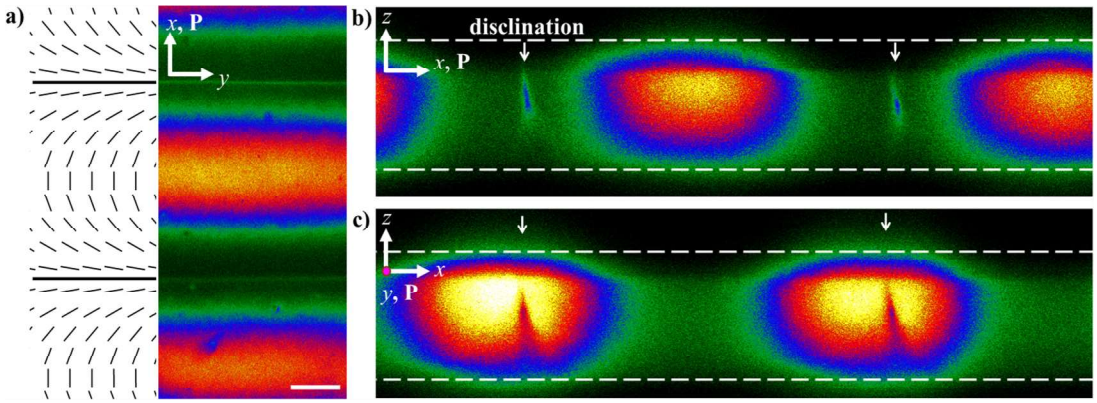

FIG. 3. PFS LCE coating. FCPM textures of (a) xy-scan with light polarized along the x-direction; sharp horizontal lines are disclinations. Scale bar 20 μm; (b) xz-scan with light polarized along the x-direction; (c) xz-scan with light polarized along the y-direction. The dotted lines in panels (b) and (c) represent the coating thickness of 17.5 μm. The white arrows in panels (b) and (c) point toward the disclination cores.

regions of splay. The contrast is opposite in Fig. 3(c), as it should be, since the polarizer is now parallel to the y axis. The FCPM signal intensity in Fig. 3(c) is weaker underneath the disclination cores and stronger in the top part of the coating. This difference correlates with the director orientation predominantly along the x axis below the disclination and along the y axis above the disclination. Both vertical scans in Figs. 3(b) and 3(c) reveal that the z-position of the disclinations is not exactly in the center of the LCE coating but shifted upwards toward the free photopatterned surface. An interesting feature of Fig. 3(c) is that the lobes to the right and to the left of the disclinations are not the mirror images of each other. This asymmetry is observed also in the temperature-triggered profile changes of the LCE coatings and can be associated with several reasons. (1) The parity can be violated by a small twist of the top plate with respect to the bottom plate so that the "C"-stripes at one plate are not exactly orthogonal to the uniform director at the other plate. (2) Asymmetry can be induced during the cooling of the isotropic phase to the nematic, since the nucleating droplets might cause a local prevalence of one twist handedness over the other. (3) In a similar way, polymerization kinetics can affect symmetry, since the process is of a finite rate; note here that polymerization can also affect the position of disclinations along the z axis. (4) Even minute amounts of chiral substances could cause a disbalance of left-handed and right-handed twists. (5) The parity can also be violated by shear deformations during the removal of one plate in the process of preparation of the LCE coating with one free surface. Peeling perpendicular to the stripes would maximize this effect, although peeling along the stripes might still produce an asymmetry because of (1)–(4) reasons.

2. Thermally controlled surface profile of LCE coatings with disclinations

In this section, we present the results for the LCE coatings of thickness $d = 5\,\mu$m, Fig. 4, and $7\,\mu$m, Figs. 5 and 6. The surface profile at 25 °C is practically flat, Figs. 4(b)–4(e), with small inhomogeneities apparently caused by the separation of the two glass plates after the polymerization and by changes in the sample temperature during preparation. As the coating is heated, the free surface develops linear microchannels-indentations above the disclination cores in both the PFS and UFS geometries, Figs. 4 and 5. These "valleys" are located in the regions where the in-plane director experience splay, i.e., at $x = \pm L/2,\ \pm 3L/2,\ \ldots$; accordingly, the bend regions at $x = 0,\ \pm L,\ \pm 2L,\ \ldots$ show elevations. The PFS coatings show deeper microchannels [Figs. 4(c) and 4(e)] as compared to the UFS coatings [Figs. 4(b) and 4(d)]. In both cases, the increase in the "C"-stripe's period diminishes the depth. For example, the coatings with $L = 80\ \mu$m show microchannels that are ~10%–30% shallower than those in the coatings with $L = 40\ \mu$m [compare Figs. 4(b) and 4(d) to Figs. 4(c) and 4(e)]. The effect is explained by the weaker gradients of the director in the stripe pattern of a larger period.

The surface profile of LCE microchannels above disclinations can be of two types, either with a single minimum, or with a double minimum, Fig. 5. Surface topographies with one minimum depicted in Figs. 5(a) and 5(c) are more frequent, while the surface topographies with a double minimum [Figs. 5(b) and 5(d)] develop ~5% of the time. As shown in the theoretical part, the double vs single valley prevalence is very sensitive to minute changes in the z-coordinate of the disclinations. Given the similarity in the thickness of coatings and temperature change protocol, the difference in

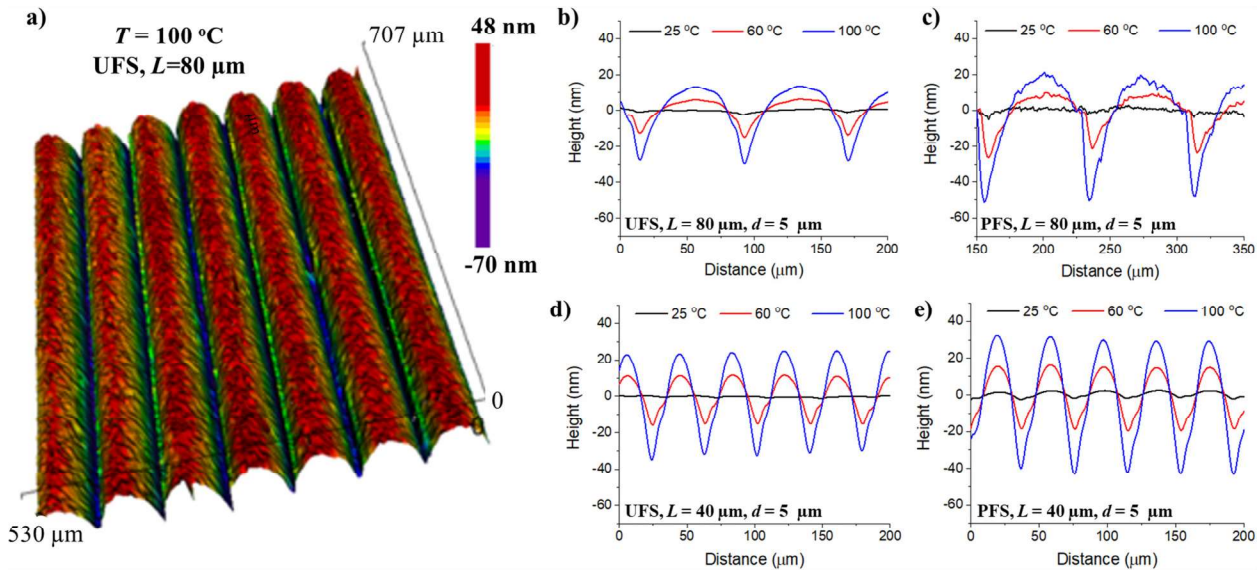

FIG. 4. (a) 3D Zygo image of UFS LCE coating at 100 °C, $L = 80\ \mu$m. Temperature dependence of LCE surface profiles of (b) UFS, $L = 80\ \mu$m; (c) PFS, $L = 80\ \mu$m; (d) USF, $L = 40\ \mu$m; (e) PFS, $L = 40\ \mu$m. In all cases, $d = 5\ \mu$m.

single-double valleys outcomes is most likely related to the details of photopolymerization kinetics, such as the z-dependent rate of polymerization, that might shift the z-positions of disclinations.

As clear from the comparison of Figs. 4(c) and 5(d), an increase of the LCE coating thickness d leads to a higher amplitude of surface deformation. For the PFS case with the period $L = 80\,\mu$m, the difference between the lowest and highest points of the free surface is $\sim$70 nm for $d = 5\,\mu$m and $\sim$150 nm for $d = 7\,\mu$m. The trend, together with the qualitative features such as the locations of valleys at $x = \pm L/2,\ \pm 3L/2,\ \ldots$, and elevations at $x = 0,\ \pm L,\ \pm 2L,\ \ldots$, is preserved in thicker coatings with $d = 17.5\,\mu$m, $L = 80\,\mu$m, where the difference is $\sim$330 nm.

Besides the out-of-plane displacements, the coatings also develop in-plane displacements. In order to observe these, we draw a straight line with a marker across the "C"-stripes of a room-temperature sample [Fig. 6(a)], at a location that is shifted from the center of the coating by approximately 25% of the sample width. In Fig. 1(a), this location would correspond to the ordinate $y \approx (210$–$260)\ \mu$m. As the temperature of the coating increases, the straight line develops a wavy shape [Fig. 6(b)], indicating displacements of a few micrometers along the y axis in the plane of the coating. Note that the marker line shifts to the left in the splay regions with disclinations and to the right in the bend regions [Fig. 6(b)].

The in-plane shifts of the coating material in Fig. 6(b) are consistent with the predictions based on the spatial dependence of the activation force,[24] which writes for the case of PFS as

$$\mathbf{f}(x, y, z = d) = \alpha|\Delta S|(\hat{\mathbf{n}}\,\mathrm{div}\,\hat{\mathbf{n}} - \hat{\mathbf{n}} \times \mathrm{curl}\,\hat{\mathbf{n}}), \tag{2}$$

where the director field $\hat{\mathbf{n}}\ (x, y, z = d)$ is specified by Eq. (1). Substituting the director field, Eq. (1), into Eq. (2), with $\alpha > 0$, one finds that the force $\mathbf{f}$, acting at the PFS of a heated coating, points toward the negative end of the y axis in the splay regions and along its positive end in the bend regions, Fig. 6(c), thus explaining the material shifts observed in Fig. 6(b). Moreover, the pattern in Fig. 6(c) also shows the activation force directed away from the splay regions ($x = \pm L/2,\ \pm 3L/2,\ \ldots$) toward the bend regions ($x = 0,\ \pm L,\ \pm 2L,\ \ldots$), which suggests formation of valleys in the splay regions and elevations in the bend regions, again in agreement with the experimental data in Figs. 4 and 5. As we shall see in Sec. III B, linear elastic theory and numerical simulations capture well not only these qualitative features but also provide a detailed quantitative description of both the in-plane and out-of-plane profile modifications of the LCE coatings.

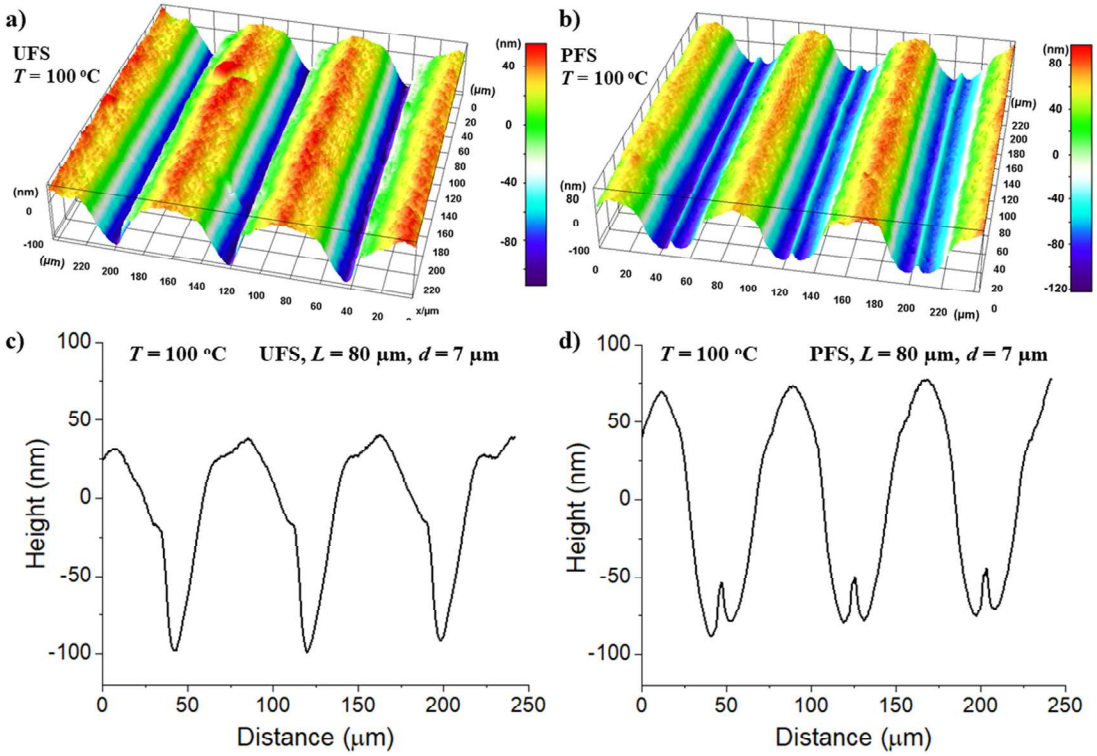

FIG. 5. DHM images of (a) UFS with one minimum and (b) PFS with double minimum surface topographies at 100 °C. Surface profiles of (c) UFS and (d) PFS coatings, $L = 80\,\mu$m at 100 °C. In all cases, $d = 7\,\mu$m.

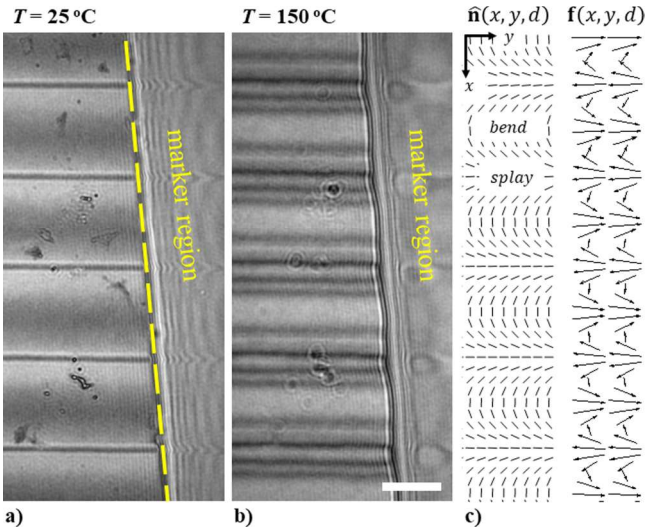

FIG. 6. (a) Straight marker line traced on top of the PFS LCE coating at 25 °C; $d = 7\,\mu$m; (b) Wavy appearance of initially straight line in panel (a) when LCE coating is heated to 150 °C. Note that the marker line shifts to the left in the splay regions with disclinations. Scale bar, 25 μm; (c) spatial variation of the director field $\hat{\mathbf{n}}$ and the activation force $\mathbf{f}$ at the patterned surface of an LCE coating upon heating; $\mathbf{f}$ points to the right in bend regions, to the left in the splay regions and from splay to bend regions, which explains qualitatively the experimental data on in-plane and out-of-plane profile shifts of the LCE coatings.

B. Theory

To understand this system theoretically, we must consider two issues. First, before crosslinking, what is the director configuration inside the liquid crystal? Second, after crosslinking, how does a liquid crystal elastomer with that director configuration respond to a change of temperature? In this section, we address each of those issues in turn. The topographic analysis of LCE coatings shows that in the explored range of thicknesses, 5–17.5 μm, the qualitative features of their profiles remain the same. Because of this, and since most of the data in the experimental section are presented for $d = 5, 7\,\mu$m, some results of the theoretical modeling below is presented for the intermediate value $d = 6\,\mu$m.

1. Director configuration: Approximate analytic calculation

We consider a nematic in a cell of thickness d, between two substrates with strong anchoring conditions. The top surface is patterned with a period L, so that $\hat{\mathbf{n}}(x, y, d) = (\cos\frac{\pi x}{L}, \sin\frac{\pi x}{L}, 0)$, and the bottom surface is uniform with $\hat{\mathbf{n}}(x, y, 0) = (1, 0, 0)$. We need to calculate the director configuration in the interior of the cell, and this configuration must have an array of twist disclinations.

As a first approximation, to obtain an analytic expression for the director field, we assume that the elastic constants of the liquid crystal are equal, and that the director field is in the xy plane and is independent of y so that $\hat{\mathbf{n}}(x, z) = (\cos\phi(x, z), \sin\phi(x, z), 0)$, where ϕ is the azimuthal angle. Based on those assumptions, the Frank–Oseen free energy becomes $F = \int d^3r \frac{1}{2}K|\nabla\phi|^2$. Minimizing this free energy over functions $\phi(x, z)$ gives the Euler–Lagrange equation $\nabla^2\phi = 0$. We solve this equation for $\phi(x, z)$ in the domain $0 \le z \le d$ and $0 \le x \le L$, and then repeat the solution for $\hat{\mathbf{n}}(x, z)$ periodically in x. In this domain, the boundary conditions can be expressed as $\phi(x, d) = \frac{\pi x}{L}$, $\phi(x, 0) = 0$ for $0 \le x \le \frac{L}{2}$, and $\phi(x, 0) = \pi$ for $\frac{L}{2} \le x \le L$. An exact solution can be found by the method of conformal mapping, following the analysis of Wang *et al*,[34] which gives

$$\phi(x, z) = \frac{1}{2}\left[\tan^{-1}\left(\frac{\cos\frac{\pi z}{d}\cosh\left[\frac{\pi}{d}\left(x - \frac{L}{2}\right)\right] - \cos\frac{\pi z_{\text{defect}}}{d}}{\sin\frac{\pi z}{d}\sinh\left[\frac{\pi}{d}\left(x - \frac{L}{2}\right)\right]}\right) + \frac{\pi}{2}\,\text{sign}\left(x - \frac{L}{2}\right)\right] + \frac{\pi z}{dL}\left(x - \frac{L}{2}\right) + \frac{\pi}{2}, \tag{3}$$

where z_{defect} is the height of the disclination above the bottom surface.

To determine the optimal height, we insert this solution into the Frank–Oseen free energy, integrate numerically over the full domain (except a small core around the disclination), and minimize over z_{defect}. For cell thickness $d = 6\,\mu$m and period $L = 40\,\mu$m, this numerical minimization gives $z_{\text{defect}} = 3.7\,\mu$m, which means that the disclination cores are located closer to the PFS surface than to the uniformly aligned bottom substrate, in agreement with the FCPM experimental data on PFS coatings, Fig. 3. For $d = 6\,\mu$m and $L = 80\,\mu$m, it yields $z_{\text{defect}} = 3.3\,\mu$m. If the cell geometry is reversed, so that the top surface is uniform and the bottom surface is patterned, then the solution is also reversed. In that case, z is replaced by $(d - z)$, and z_{defect} by $(d - z_{\text{defect}})$. We recognize that the disclinations may be at a different height, either because of elastic properties of the nematic or because of the dynamics of the photopolymerization process. For that reason, we keep z_{defect} as a free parameter so that we can see the effect of varying the disclination height.

2. Director configuration: Finite difference method

To go beyond the approximations of the analytic calculation, we simulate the director configuration in the nematic cell using a finite difference method (FDM). For this simulation, we use a lattice spacing of 0.25 μm, and assume infinitely strong anchoring

as stated above. We relax the director field to minimize the full Frank–Oseen free energy,

$$F = \int_V d^3r \left[\frac{1}{2}K_{11}(\mathrm{div}\,\hat{\mathbf{n}})^2 + \frac{1}{2}K_{22}(\hat{\mathbf{n}}\cdot\mathrm{curl}\,\hat{\mathbf{n}})^2 + \frac{1}{2}K_{33}(\hat{\mathbf{n}}\times\mathrm{curl}\,\hat{\mathbf{n}})^2\right] - \int_S d^2r \left[\frac{1}{2}(K_{22}+K_{24})\hat{\mathbf{N}}\cdot(\hat{\mathbf{n}}\mathrm{div}\,\hat{\mathbf{n}} + \hat{\mathbf{n}}\times\mathrm{curl}\,\hat{\mathbf{n}})\right]. \tag{4}$$

Here, the first three terms represent the elastic free energy of splay, twist, and bend, respectively. The last term is the saddle-splay free energy, the saddle-splay elastic constant K_{24}, which is represented as an integral over the confining surface, where $\hat{\mathbf{N}}$ is the unit vector normal to the surface.[38] We use the elastic constants $K_{11} = 6.01$ pN, $K_{22} = 3.83$ pN, $K_{24} = 5.97$ pN, and $K_{33} = 8.56$ pN, associated with the common liquid crystal 5CB at room temperature, which is similar to the experimental material.[39] To avoid getting trapped in a metastable state, we add thermal noise to the system.

Figure 7(a) shows that the disclination core, represented as a black circle, is located closer to the photopatterned surface. When using $d = 5\ \mu$m and $L = 40\,\mu$m, the result is similar to the analytic calculation above and $z_{\mathrm{defect}} \approx 4\,\mu$m. The precise location is higher than in the analytic calculation because of the different elastic constants. In Fig. 7(b), the 3D visualization of the Frank free energy density shows that the highest energy occurs at the disclination line.

3. Shape change: Linear elasticity theory

We now suppose that a nematic with the director configuration calculated above is crosslinked to form an LCE film. Because of the crosslinking, the director configuration cannot change. We further suppose that one side of the elastomer film is rigidly attached to a substrate, so that it cannot deform, while the other side is free. If the temperature increases, the scalar order parameter of the material decreases, and hence the elastomer tends to contract parallel and expand perpendicular to the local director. We would like to calculate the final shape of the film.

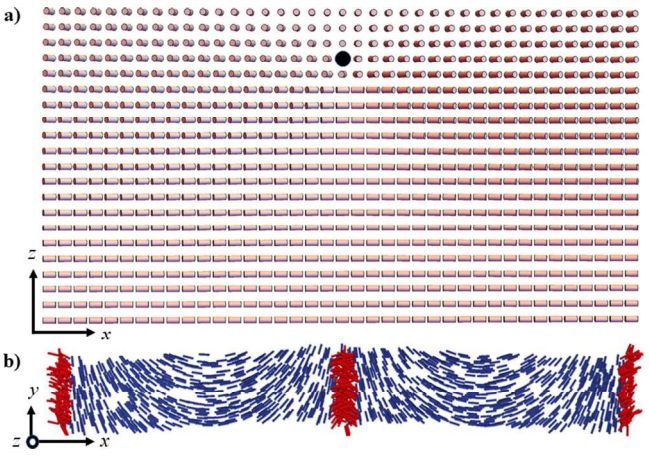

FIG. 7. (a) xz-cross section showing that the disclination line (z_{defect}, represented as a black circle) is located closer to the photopatterned substrate, (b) 3D-visualization of Frank free energy density map, illustrating the highest values in red.

As a first approximation, we address this question using linear elasticity theory. Indeed, this problem is particularly suitable for linear elasticity theory, because the rigid attachment to the substrate prevents large elastic deformations.

In linear elasticity theory, we suppose that the material deformation is characterized by a 3D displacement field $\mathbf{u}(x, y, z)$. On the bottom surface $z = 0$, the rigid attachment implies the boundary condition $\mathbf{u}(x, y, 0) = 0$. On the top surface $z = d$, we would like to calculate the displacement field $\mathbf{u}(x, y, d)$, which includes both horizontal and vertical displacements. For this calculation, we define the linear strain tensor $\epsilon_{ij} = \frac{1}{2}(\partial_i u_j + \partial_j u_i)$. We assume that the material is incompressible, so that the local volume change is $Tr(\boldsymbol{\epsilon}) = \partial_i u_i = 0$. In that case, the elastic free energy becomes

$$F = \int dxdy \int_0^d dz(\mu\epsilon_{ij}\epsilon_{ij} - \alpha\Delta Q_{ij}\epsilon_{ij}). \tag{5}$$

Here, the first term is the energy cost of a shear deformation, with shear modulus μ, and the second term is the coupling between the strain ϵ_{ij} and changes in nematic order $\Delta Q_{ij} = \Delta S\left(\frac{3}{2}n_i n_j - \frac{1}{2}\delta_{ij}\right)$, with the coupling constant $\alpha > 0$. In a heating experiment, the change in nematic order is $\Delta S < 0$.

As an approximation, we consider a sample that is infinite in the y direction. Because the director is independent of y, the displacement field should also be independent of y. Across the small film thickness d, we assume the simple variation $u(x, z) = \left(a_x(x)z,\ a_y(x)z,\ -\frac{1}{2}(\partial_x a_x)z^2\right)$, which satisfies the boundary condition and the incompressibility constraint. We insert that assumption into the elastic free energy and integrate over z to obtain an effective 2D free energy. Minimizing that expression over the two functions $a_x(x)$ and $a_y(x)$ gives the Euler-Lagrange equations,

$$\begin{aligned} a_x - \frac{5d^2}{3}\frac{\partial^2 a_x}{\partial x^2} + \frac{d^4}{20}\frac{\partial^4 a_x}{\partial x^4} &= -\frac{\alpha}{d\mu}\frac{\partial \Delta Q_{xx}^{\mathrm{moment}}}{\partial x} = \frac{1}{d\mu}f_x^{\mathrm{moment}}, \\ a_y - \frac{d^2}{3}\frac{\partial^2 a_y}{\partial x^2} &= -\frac{\alpha}{d\mu}\frac{\partial \Delta Q_{xy}^{\mathrm{moment}}}{\partial x} = \frac{1}{d\mu}f_y^{\mathrm{moment}}, \end{aligned} \tag{6}$$

where $\Delta Q_{ij}^{\mathrm{moment}}(x) = \int_0^d z\,\Delta Q_{ij}(x, z)\,dz$. Hence, the material responds to the first moment of the change in nematic order so that changes near the top surface have stronger effects than changes near the bottom surface. The expressions on the right side of the equations can be simplified in terms of the activation force field defined by Babakhanova *et al.*,[24] which is $f_j = -\alpha\partial_i(\Delta Q_{ij})$, with $\mathbf{f}^{\mathrm{moment}}(x) = \int_0^d z\,\mathbf{f}(x, z)\,dz$. Thus, this vector field is the relevant stimulus on the material.

To solve the Euler–Lagrange equations, we express the stimulus as a Fourier series $\mathbf{f}^{\mathrm{moment}}(x) = \sum_q \mathbf{f}_q^{\mathrm{moment}} e^{iqx}$, where the wave number q must be an integer multiple of $2\pi/L$. We insert the approximate analytic solution of Eq. (3) for the director field into

the nematic order tensor, differentiate to find $\mathbf{f}(x, z)$, integrate numerically over z to obtain $\mathbf{f}^{\text{moment}}(x)$, and then integrate numerically over x to calculate the Fourier coefficients $\mathbf{f}_q^{\text{moment}}$. The sums include the first 50 terms of the Fourier series, which give an excellent representation of $\mathbf{f}^{\text{moment}}(x)$. We then obtain the solution

$$a_x(x) = \frac{1}{d\mu}\sum_q \frac{60}{60 + 100d^2q^2 + 3d^4q^4} f_{q,x}^{\text{moment}} e^{iqx},$$
$$a_y(x) = \frac{1}{d\mu}\sum_q \frac{3}{3 + d^2q^2} f_{q,y}^{\text{moment}} e^{iqx}. \tag{7}$$

From this solution for $a_x(x)$ and $a_y(x)$, we obtain the displacement throughout the sample. In particular, we find the horizontal and vertical components of the displacement $u(x, y, d)$ on the top surface.

As a specific example, we calculate the displacement for a patterned-free-surface LCE coating with thickness $d = 6\,\mu$m and period $L = 40\,\mu$m. Figure 8 shows the in-plane displacements. This figure is calculated assuming a disclination height of $z_{\text{defect}} = 3\,\mu$m, but the in-plane displacements are not sensitive to z_{defect}. The material shifts outward and toward $-y$ in the splay regions above the disclinations, for $x \approx \pm L/2$, $\pm 3L/2$, …, and it shifts inward and toward $+y$ in the bend regions, for $x \approx 0$, $\pm L$, …, in agreement with the qualitative scheme of the activation force in Fig. 6(c). The maximum in-plane displacement is $(u_y^{\max} - u_y^{\min}) = (3.7\,\mu\text{m}) \times (\alpha|\Delta S|/\mu)$. By comparison, in Fig. 6(b), the experimental in-plane displacement is ~3 μm. Hence, we can tentatively estimate that the dimensionless ratio $\alpha|\Delta S|/\mu$ is in the range of 0.1 to 1 in the experiment.

Figure 9(a) shows the out-of-plane displacements. Unlike the in-plane displacements, the out-of-plane displacements are quite sensitive to z_{defect}. To illustrate this dependence, the figure shows several values of z_{defect} from 1 to 5 μm. For low z_{defect}, when the disclinations are close to the uniform fixed surface, the material is depressed in a single valley above the each disclination, similar to Figs. 4(a) and 4(c). By contrast, for high z_{defect}, when the disclinations are close to the patterned free surface, each valley splits into two parallel valleys, with a ridge directly above each disclination, similar to the experimental profile in Figs. 5(b) and 5(d).

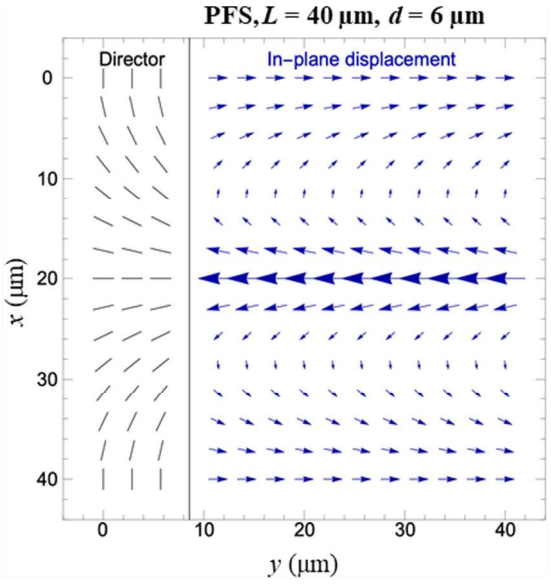

FIG. 8. Linear elasticity theory calculations of in-plane displacements of the heat-activated PFS LCE coating with "C"-stripe period of $L = 40\,\mu$m, thickness $d = 6\,\mu$m, and disclination height $z_{\text{defect}} = 3\,\mu$m.

We can now use the same approximate analytic solution to determine the effects of changing different parameters in the experimental geometry. To see the effect of the period L, Fig. 9(b) shows the corresponding out-of-plane displacements for $L = 80\,\mu$m. In this case, there is more of a tendency toward split valleys, which begin at a lower value of z_{defect}. The width of the valleys is comparable to the thickness $d = 6\,\mu$m. The valleys appear wider in Fig. 9(a) than in Fig. 9(b) only because the ratio d/L is smaller in the second case than the first.

To see the effect of patterned vs uniform free surface, Figs. 9(c) and 9(d) show the analogous results for the uniform-free-surface LCE coating. In those cases, the material is depressed in a single valley above each disclination when z_{defect} is high, close to the uniform free surface. By contrast, each valley splits into two parallel valleys when z_{defect} is low, close to the patterned fixed surface. (The in-plane displacements for these cases are not shown, because they are generally similar to Fig. 8.) Figure 9 thus establishes that the double-minimum profile of microchannels develops each time the disclination is close to the patterned surface, regardless of whether this surface is free or not.

The LCE profiles in Fig. 9 are shown in micrometer units with a dimensionless factor $\alpha|\Delta S|/\mu$. Since the out-of-plane displacements of the LCEs are better resolved in the experiments, Figs. 4 and 5, as compared to their in-plane counterparts, Fig. 6(b), it is of interest to estimate $\alpha|\Delta S|/\mu$ by comparing Fig. 9 to Figs. 4 and 5. For the PFS coating with $d = 6\,\mu$m, $L = 80\,\mu$m, the difference between the lowest and highest points of the profiles in Fig. 9(b), $(u_z^{\max} - u_z^{\min}) = (230 - 500)\,\text{nm} \times (\alpha|\Delta S|/\mu)$, while the similar quantity in the experiment, taken as an average of $(u_z^{\max} - u_z^{\min}) \approx 70\,\text{nm}$ in Fig. 4(c) for $d = 5\,\mu$m and $(u_z^{\max} - u_z^{\min}) \approx 150\,\text{nm}$ in Fig. 5(d) for $d = 7\,\mu$m, is about 110 nm. Therefore, $\alpha|\Delta S|/\mu$ for the explored material and the range of temperature changes is expected to be in the range of 0.2–0.5.

4. Shape change: Finite element modeling (FEM)

We model a nematic elastomer thin film with a 3D tetrahedral mesh with physical dimensions of $L_x = 200\,\mu$m (5 × periodicity of the "C"-stripe pattern), $L_y = 50\,\mu$m and the thickness of an LCE coating $d = 5\,\mu$m. We assumed that the material density = 1.2 g/cm^3 and shear modulus = 0.57 MPa. The thermo-mechanical response is modeled via the Hamiltonian of the form

$$H = \frac{1}{2}\sum_t V^t C_{ijkl}\varepsilon_{ij}^t\varepsilon_{kl}^t - \alpha\sum_t V^t\varepsilon_{ij}^t(S^t - S^0)\frac{1}{2}(3n_i^t n_j^t - \delta_{ij}) + \frac{1}{2}\sum_p m_p v_p^2. \tag{8}$$

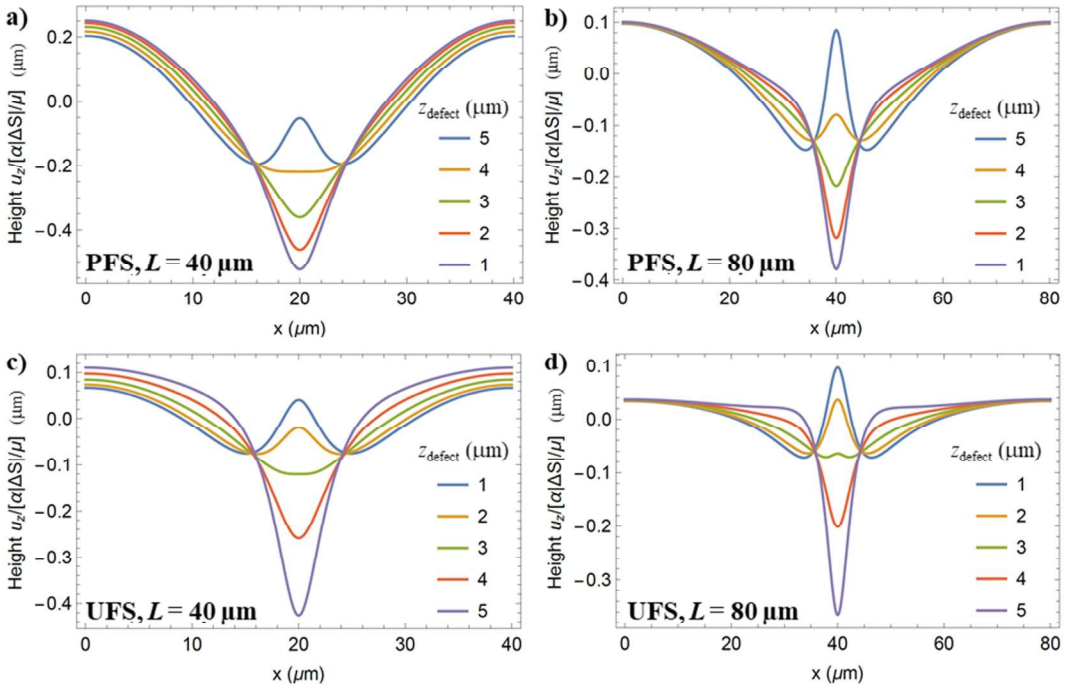

FIG. 9. Linear elasticity theory calculations of out-of-plane displacements of heat-activated LCE coatings with thickness $d = 6\,\mu$m. These examples show (a), (b) PFS vs (c), (d) UFS, "C"-stripe period (a), (c) $L = 40\,\mu$m vs (b), (d) $80\,\mu$m, for several values of the disclination height z_{defect}. The predicted out-of-plane displacements are the numbers on the vertical axis, times the dimensionless ratio $\alpha|\Delta S|/\mu$, in units of μm.

Here, the first term represents the elastic strain energy summed over elements t, where ε_{ij} is the Green–Lagrange strain, C_{ijkl} is a tensor of elastic constants, and V^t is the volume of element t in the reference state. The second term represents the coupling of strain and nematic order, with coupling coefficient α, and where S^t is the nematic scalar order parameter in element t and S° is the value at the temperature where the sample is in its strain-free reference state. The final term is the kinetic energy in the lumped-mass approximation, with mass m_p and instantaneous velocity v_p of each node p. To represent an increase in the temperature, we gradually reduce the scalar order parameter in each element by a total amount ΔS over 10 000 time steps. Then, we hold the scalar order parameter fixed for an additional 5000 time steps and allow the sample to relax to mechanical equilibrium by applying a dissipative force to each node proportional to its velocity. The simulation ends when the sample has come to mechanical equilibrium. Total change ΔS matches experimental data from our Berek compensator measurements of $\Delta S \approx -0.2$. The nematic director $\hat{\mathbf{n}}$ within each element is "blueprinted" using the computational solution found via FDM, interpolated to the unstructured finite element mesh.

As shown in Fig. 10, the results of the FEM simulations agree with the experimental data and confirm that upon actuation of an LCE coating that contains linear disclinations, the amplitude of deformation is higher in the case of PFS [Figs. 10(a), 10(c) and 10(e)] as compared to UFS [Figs. 10(b), 10(d) and 10(f)]. Channel shape in the middle of the sample, Figs. 10(b) and 10(d), as predicted by FEM agrees well with geometries observed in experiment and predicted by linear elasticity calculations. Taking 3D effects and nonlinear elasticity into account, we find that elastic relaxation near free surfaces at the edges of the sample induces significant local modification of channel structure, Figs. 10(a), 10(b), 10(e), and 10(f). FEM simulations also demonstrate in-plane displacements consistent with experimental observations in Fig. 6(b) and with the qualitative scheme of the activation force in Fig. 6(c); the amplitude of shifts is higher for the patterned free surface geometry.

Besides capturing the qualitative features, the FEM simulations provide a good quantitative description of the dynamic profiles of the LCE coatings. The simulations performed for $d = 5\,\mu$m, $L = 40\,\mu$m, show that as the dimensionless factor $\alpha|\Delta S|/\mu$ increases from 0.35 to 1, the out-of-plane displacement amplitude $(u_z^{\max} - u_z^{\min})$ grows from 43 nm to 132 nm for UFS and from 53 nm to 174 nm for PFS. The experimental amplitudes for the coatings of the same periodicity and thickness, are ≈60 nm for UFS, Fig. 4(d), and ≈70 nm for PFS, Fig. 4(e). The best numerical agreement with the experiments is achieved for $\alpha|\Delta S|/\mu \approx 0.45 - 0.49$, which narrows down the range of 0.2–0.5 presented above in the section on linear elasticity. The FEM results in Fig. 10 are presented for $\alpha|\Delta S|/\mu \approx 0.46$, in which case the FEM simulations yield $(u_z^{\max} - u_z^{\min}) \approx 56$ nm for UFS, Fig. 10(c), and ≈71 nm for PFS, Fig. 10(d), very close to the data in Figs. 4(d) and 4(e).

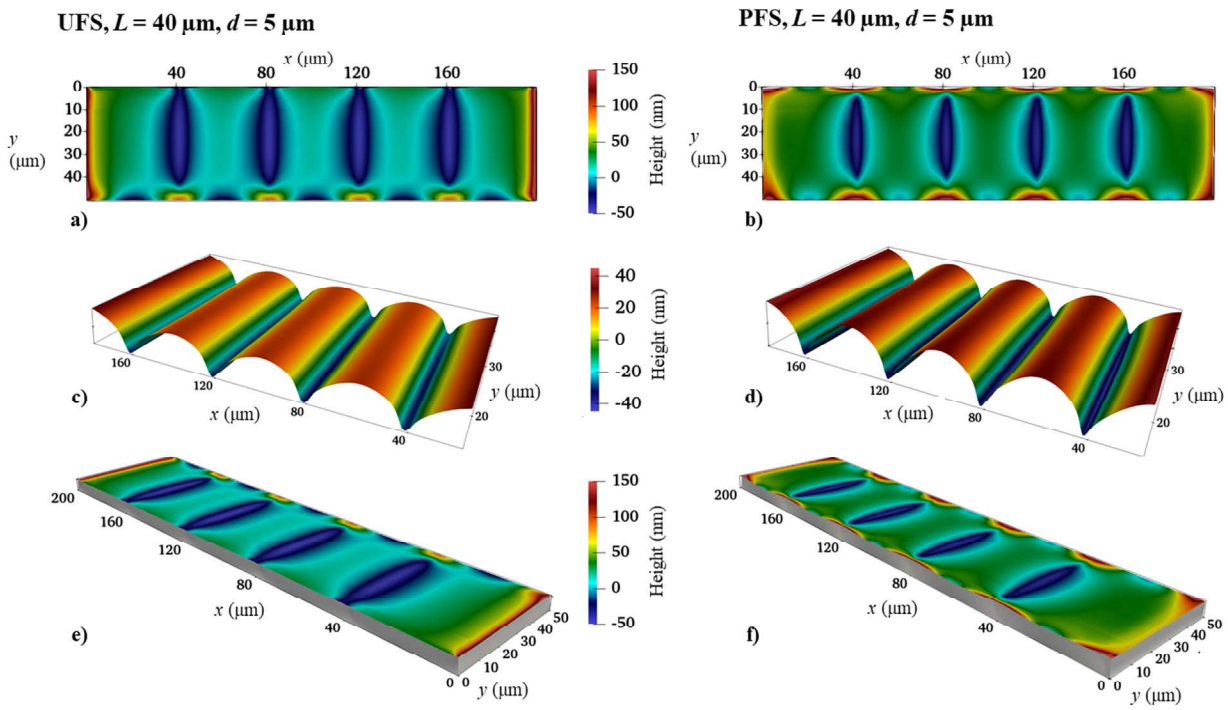

FIG. 10. FEM simulations of heat-activated LCE coating in [(a), (c), and (e)] UFS and [(b), (d), and (f)] PFS configurations. (a) and (b): Out-of-plane displacements (top view). (c) and (d): 3D views of the LCE surface profile in the center of the sample, away from the edges. (e) and (f): 3D views of the entire samples. Vertical displacements along the normal to the coating are shown in pseudocolors. Coatings' edges are modified by the elastic relaxation near the free surfaces; because of this finite-size effect, the experimental data in Figs. 4(d) and 4(e) should be compared to the profiles in the center of the coatings shown in parts (c) and (d), where the amplitude of out-of-plane displacement is 56 nm for UPS (c), and 71 nm for PFS (d). The in-plane displacements are larger for the PFS and give rise to a rippled structure along the sample edges.

IV. CONCLUSION

Understanding the relationship between the dynamics of responsive materials such as LCEs and their ordering is of prime importance in fundamental physics of out-of-equilibrium systems. Many facets of the activity-orientational order coupling can be studied in a controlled manner by using predesigned patterns of the orientational order with topological defects as an integral part of the system. In this work, we demonstrate a deterministic relationship between the complex three-dimensional geometry of the preinscribed molecular orientation and the dynamic surface topography of the disclination-containing thermally activated LCE coatings. The disclinations are predesigned by confining the nematic monomer between two plates with different in-plane director patterns, one unidirectional and the other periodically distorted with alternating splay and bend in the shape of the letter "C," resembling Néel walls. The disclinations form in response to the antagonostic boundary conditions as singular lines that run in the bulk of the sample parallel to the bounding plates, resolving frustrations in the regions in which the top and bottom directors are perpendicular to each other. The preferred location of disclinations is shifted from the midplane of the cell toward the patterned substrate. Qualitatively, it implies that the elastic costs of different director deformations, namely, the surface-imposed splay-bend and distortions around the disclinations "cancel" each other; for other examples of such cancellations, see Refs. 40 and 41. The shift appears to be universal for both monomeric and polymerized nematic liquid crystals. In the cross-linked system, the shift of disclinations from the middle plane can be additionally affected by the kinetics of polymerization.

The LCE coatings prepared at room temperature with a system of disclinations are initially flat. Once the coatings are heated, a decrease in the scalar order parameter coupled to director distortions produces a profound change in the topography of the coating. Namely, the thickness of the coatings decreases along the vertical planes that contain disclinations (thus forming microgrooves) and increases in the intermediate locations, where the director is uniform along the normal to the coating. In terms of the director pattern predesigned on one of the surfaces, Eq. (1), the microchannels-valleys form along the splay regions and elevations run along the bend regions. Besides the displacements along the normal direction, the LCE coatings show also in-plane displacements. The correspondence between the directions of profile shifts, both out-of-plane deflections and in-plane material displacements, is easy to trace qualitatively by considering the spatial variation of the activation force $\mathbf{f}$, Eq. (2) and Fig. 6(c). The profile of the LCE coating with periodic valleys above the disclinations can be of two types: single-minimum valleys and double-minimum valleys.

The latter form when the disclinations are close to the patterned surface of a heated coating.

The experimentally observed modifications of the LCE profiles in response to the temperature are reproduced in detail by the linear elasticity theory and by nonlinear finite-element numerical simulations that predict a variety of outcomes, including the single and double valleys. The comparison of the experimental data in Figs. 4 and 5 and the linear theory, Fig. 9, leads to an estimate that the dimensionless ratio $\alpha|\Delta S|/\mu$ characterizing the material and the range of temperature change is in the range of 0.2–0.5. The nonlinear numerical simulations narrow this range down to 0.45–0.49. The estimate agrees with the suggestion[23] that the quantity $\alpha|\Delta S|/\mu$ is of the order of $|l_{\parallel}-l_{\perp}|/\langle l\rangle$, where $l_{\parallel}$ and $l_{\perp}$ are the typical lengths of the polymer segments connecting cross-linked points along the director and perpendicular to it, respectively, and $\langle l\rangle$ is the average segment length.

Note here that the theory and simulations used only approximate rather than experimentally measured values of some material parameters. For example, simulations of the director field employ the Frank elastic constants known for the conventional nematic 5CB but not for the monomeric composition shown in Figs. 2(b)–2(f), since for the latter, the data are not available. Furthermore, director surface anchoring strength at interfaces is always finite in laboratory samples, while the modeling assumes an infinitely strong anchoring. Despite these limitations, the experiment, theory, and simulations are very close in the description of the profile changes of the LCE coatings. The good correspondence suggests that the decisive factor in shaping the profile of the coating during heating is the activation force field $\mathbf{f}=\alpha|\Delta S|(\,\hat{\mathbf{n}}\mathrm{div}\,\hat{\mathbf{n}}-\hat{\mathbf{n}}\times\mathrm{curl}\,\hat{\mathbf{n}})$ that explains both in-plane and out-of-plane shifts of the material with a pre-patterned director field. Small variations in film thickness, elastic constants, or surface anchoring play a less significant role.

Qualitatively, the development of valleys at elevated temperatures can be understood as thickening of the film along the nearby locations where the director does not change along the z axis. In these locations, the ellipsoid of the nematic order parameter becomes less elongated and approaches a sphere upon heating, which implies thickening of the film. The conservation of mass means that the regions with disclinations develop valleys. Both the experiments and the theory demonstrate that the director distortions produce not only out-of-plane deflections but also in-plane mass transport, guided by the director pattern. The theoretical and numerical models predict not only the correct direction of material shifts but also quantify these shifts in terms of the elastic paremeters of the LCE and changes of the scalar order parameter.

The described dynamic profile of the patterned LCE coatings should be distinguished from the wrinkles that LCE coatings and films develop under an external mechanical loading, even when the director is initially uniform in space and the load is unidirectional; this wrinkling effect has been studied extensively, see the most recent papers[42–46] and references therein. In the present paper, the reason for surface modulations is not an external load: it is the pre-patterned director gradients that yield a non-flat surface topography once the change in the scalar order parameter is activated by the temperture, which is an external action of a scalar isotropic nature with no preferred direction in space.

The work demonstrates that the geometry and amplitude of surface deformations in LCE coatings activated by an external cue such as temperature can be controlled by the gradients of director distortions at singular disclinations. The established close correspondence between the experiment and theory suggests that the proposed linear elasticity theory and nonlinear finite-element numerical simulations grasp the most salient details of responsive patterned LCEs and can be used to model other complicated geometries, in which the thermal, electromagnetic, or chemical energy can be transformed into elastic response and potentially useful mechanical work.

ACKNOWLEDGMENTS

The work was funded by the Office of Science, U.S. Department of Energy, under Grant No. DE-SC0019105 (LCE coating design, preparation, characterization, plasmonic masks fabrication), and by the National Science Foundation (NSF) under Grant Nos. CMMI-1663041 and DMR-1409658 (LCE theory and simulations). The authors thank Dr. T. Turiv for helpful discussions, and Dr. Barbary Tury and Dr. Frank Liu for their help with the measurements.

DATA AVAILABILITY

The data that support the findings of this study are available from the corresponding author upon reasonable request.

REFERENCES

[1]P. M. Mendes, Chem. Soc. Rev. **37**(11), 2512–2529 (2008).
[2]K. S. Liu, X. Yao, and L. Jiang, Chem. Soc. Rev. **39**(8), 3240–3255 (2010).
[3]D. Q. Liu and D. J. Broer, Liq. Cryst. Rev. **1**(1), 20–28 (2013).
[4]T. J. White and D. J. Broer, Nat. Mater. **14**(11), 1087–1098 (2015).
[5]H. Shahsavan, L. Yu, A. Jákil, and B. X. Zhao, Soft Matter **13**(44), 8006–8022 (2017).
[6]D. Martella and C. Parmeggiani, Chem. Eur. J. **24**(47), 12206–12220 (2018).
[7]G. Babakhanova, J. Krieger, B. X. Li, T. Turiv, M. H. Kim, and O. D. Lavrentovich, J. Biomed. Mater. Res. A **108**(5), 1223–1230 (2020).
[8]T. Turiv, J. Krieger, G. Babakhanova, H. Yu, S. V. Shiyanovskii, Q.-H. Wei, M.-H. Kim, and O. D. Lavrentovich, Sci. Adv. **6**(20), eaaz6485 (2020).
[9]G. Koçer, J. Ter Schiphorst, M. Hendrikx, H. G. Kassa, P. Leclère, A. Schenning, and P. Jonkheijm, Adv. Mater. **29**(27), 1606407 (2017).
[10]E. M. Akinoglu, L. T. de Haan, S. R. Li, Z. K. Xian, L. L. Shui, J. W. Gao, G. F. Zhou, and M. Giersig, ACS Appl. Mater. Interface **10**(43), 37743–37748 (2018).
[11]M. J. Ford, C. P. Ambulo, T. A. Kent, E. J. Markvicka, C. F. Pan, J. Malen, T. H. Ware, and C. Majidi, Proc. Natl. Acad. Sci. U.S.A. **116**(43), 21438–21444 (2019).
[12]M. K. Abdelrahman, H. Kim, J. Maeng, P. Ondrusek, and T. H. Ware, Macromolecules **53**(7), 2388–2395 (2020).
[13]L. T. de Haan and G. F. Zhou, J. Phys. Chem. Solids **122**, 36–40 (2018).
[14]M. Kleman and O. D. Lavrentovich, *Soft Matter Physics: An Introduction* (Springer, New York, 2003).
[15]D. L. Thomsen, P. Keller, J. Naciri, R. Pink, H. Jeon, D. Shenoy, and B. R. Ratna, Macromolecules **34**(17), 5868–5875 (2001).
[16]M. Warner and E. M. Terentjev, *Liquid Crystal Elastomers* (Oxford University Press, Oxford, 2003).
[17]H. Aharoni, Y. Xia, X. Y. Zhang, R. D. Kamien, and S. Yang, Proc. Natl. Acad. Sci. U.S.A. **115**(28), 7206–7211 (2018).

[18]M. E. McConney, A. Martinez, V. P. Tondiglia, K. M. Lee, D. Langley, I. I. Smalyukh, and T. J. White, Adv. Mater. **25**(41), 5880–5885 (2013).
[19]C. Mostajeran, M. Warner, T. H. Ware, and T. J. White, Proc. Math. Phys. Eng. Sci. **472**(2189), 20160112 (2016).
[20]T. H. Ware, M. E. McConney, J. J. Wie, V. P. Tondiglia, and T. J. White, Science **347**(6225), 982–984 (2015).
[21]M. Warner, C. D. Modes, and D. Corbett, Proc. Roy. Soc. A Math. Phys. **466**(2122), 2975–2989 (2010).
[22]S. Serak, N. Tabiryan, R. Vergara, T. J. White, R. A. Vaia, and T. J. Bunning, Soft Matter **6**(4), 779–783 (2010).
[23]A. H. Gelebart, D. Jan Mulder, M. Varga, A. Konya, G. Vantomme, E. W. Meijer, R. L. B. Selinger, and D. J. Broer, Nature **546**(7660), 632–636 (2017).
[24]G. Babakhanova, T. Turiv, Y. Guo, M. Hendrikx, Q. H. Wei, A. Schenning, D. J. Broer, and O. D. Lavrentovich, Nat. Commun. **9**(1), 456 (2018).
[25]H. Kim, J. Gibson, J. M. Maeng, M. O. Saed, K. Pimentel, R. T. Rihani, J. J. Pancrazio, S. V. Georgakopoulos, and T. H. Ware, ACS Appl. Mater. Interface **11**(21), 19506–19513 (2019).
[26]G. Babakhanova, A. P. H. J. Schenning, D. J. Broer and O. D. Lavrentovich, Proc. SPIE, **10941**, 109410I (2019).
[27]G. Babakhanova, H. Yu, I. Chaganava, Q. H. Wei, P. Shiller, and O. D. Lavrentovich, ACS Appl. Mater. Interface **11**(16), 15007–15013 (2019).
[28]M. Dai, O. T. Picot, J. M. N. Verjans, L. T. de Haan, A. P. H. J. Schenning, T. Peijs, and C. W. M. Bastiaansen, ACS Appl. Mater. Interface **5**(11), 4945–4950 (2013).
[29]L. T. de Haan, J. M. N. Verjans, D. J. Broer, C. W. M. Bastiaansen, and A. P. H. J. Schenning, J. Am. Chem. Soc. **136**(30), 10585–10588 (2014).
[30]R. C. P. Verpaalen, A. E. J. Souren, M. G. Debije, T. A. P. Engels, C. W. M. Bastiaansen, and A. P. H. J. Schenning, Soft Matter **16**(11), 2753–2759 (2020).
[31]O. M. Wani, R. Verpaalen, H. Zeng, A. Priimagi, and A. Schenning, Adv. Mater. **31**(2), 1805985 (2019).
[32]W. Feng, D. J. Broer, and D. Q. Liu, Adv. Mater. **30**(11), 1704970 (2018).
[33]K. Sunami, K. Imamura, T. Ouchi, H. Yoshida, and M. Ozaki, Phys. Rev. E **97**(2), 020701 (2018).
[34]M. Wang, Y. Li, and H. Yokoyama, Nat. Commun. **8**(1), 388 (2017).
[35]Y. B. Guo, M. Jiang, C. H. Peng, K. Sun, O. Yaroshchuk, O. Lavrentovich, and Q. H. Wei, Adv. Mater. **28**(12), 2353–2358 (2016).
[36]I. I. Smalyukh, S. V. Shiyanovskii, and O. D. Lavrentovich, Chem. Phys. Lett. **336**(1–2), 88–96 (2001).
[37]O. D. Lavrentovich, Pramana J. Phys. **61**(2), 373–384 (2003).
[38]Y. B. Guo, S. Afghah, J. Xiang, O. D. Lavrentovich, R. L. B. Selinger, and Q. H. Wei, Soft Matter **12**(30), 6496 (2016).
[39]M. Cui and J. R. Kelly, Mol. Cryst. Liq. Cryst. Sci. Technol. Sect. A **331**(1), 49–57 (1999).
[40]J. V. Selinger, Liq. Cryst. Rev. **6**(2), 129–142 (2018).
[41]O. D. Lavrentovich and V. M. Pergamenshchik, Int. J. Mod. Phys. B **9**(18–19), 2389–2437 (1995).
[42]H. Soni, R. A. Pelcovits, and T. R. Powers, Phys. Rev. E **94**(1), 012701 (2016).
[43]P. Plucinsky and K. Bhattacharya, J. Mech. Phys. Solids **102**, 125–150 (2017).
[44]M. S. Krieger and M. A. Dias, Phys. Rev. E **100**(2), 022701 (2019).
[45]L. A. Mihai and A. Goriely, J. Mech. Phys. Solids **144**, 104101 (2020).
[46]Y. Liu, W. Ma, and H.-H. Dai, J. Mech. Phys. Solids **145**, 104169 (2020).